X-RAY DIFFRACTOMETER FOR THIN FILM ANALYSIS AT HOUGHTON UNIVERSITY

By

Nathaniel T. Davie

A thesis submitted in partial fulfillment of the requirements for the degree of

Bachelor of Science

Houghton University

May 2024

Signature of Author…………………………………………………………………………………..
Department of Physics
May 3, 2024

………………………………………………………………………………………………………...
Dr. Brandon Hoffman
Professor of Physics
Research Supervisor

………………………………………………………………………………………………………...
Dr. Katrina Koehler
Assistant Professor of Physics

X-RAY DIFFRACTOMETER FOR THIN FILM ANALYSIS AT HOUGHTON UNIVERSITY

By

Nathaniel T. Davie

Submitted to the Department of Physics
on May 3, 2024, in partial fulfillment of the
requirement for the degree of
Bachelor of Science

Abstract

A Bragg-Brentano theta-2 theta x-ray Diffractometer was advanced towards completion in construction at Houghton University as a means to measure the lattice structure and sub-atomic spacing of thin films and small crystals. The x-ray Diffractometer (XRD) uses angles of diffracted characteristic x-rays to analyze the space between cells. The XRD is dependent on the derivation and application of the mathematical equation denoted by Bragg's Law, stating the angle of large quantities of x-rays being delayed by integer multiples such that the wavefronts are lined up in shape, called constructive interference. The Houghton XRD machine was inherited from previous students ranging back 14 years. Preliminary tests using a Silicon thin film and a single Sodium-Iodide lab-grown crystal have been conducted, and further, intensive tests are aimed to be conducted in the fall of 2024. The analysis conducted at Houghton University by the XRD can offer a range of data regarding the mechanical, physical, and electrodynamic properties of thin films, resulting in optimized application of the thin films themselves.

Thesis Supervisor: Dr. Brandon Hoffman
Title: Professor of Physics

TABLE OF CONTENTS

TABLE OF FIGURES

Chapter 1: Background and History of XRD

1.1. *History*

1.1.1. Discovery of the X-ray

The first x-ray was discovered accidentally by Wilhelm Röntgen, a German physicist in 1895 [1]. Initially, the x-ray as considered by Röntgen was a form of excited particles infused with high levels of energy, completely mischaracterizing the electromagnetic wave. Following the research on electrons and cathode rays by J.J. Thomson in 1894 [2], Röntgen studied the effects of passing gases at low pressure through electric current. The experimental apparatus utilized by Röntgen can be seen pictured in Figure 1. When experimenting with electron discharges through the gases, Röntgen covered a glass tube with cardboard to contain the light emitted when electrons would strike the tube. Röntgen noticed a thin glass pane nearby would also glow when electrons struck the tube.

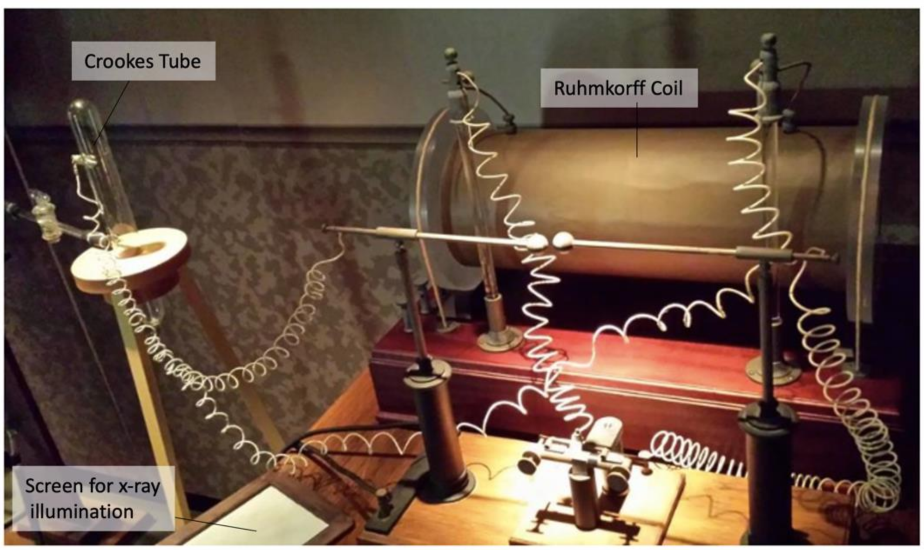

Figure 1. Replica of Röntgen x-ray experimental apparatus photograph. The Crookes tube connected to a power source, the Ruhmkorff or induction coil through its two electrodes, and generated x-rays which traveled from the tube to the illumination screen. The screen was constructed by painting a cardboard sheet with barium platinocyanide and would fluorescently illuminate when stimulated with x-rays. The apparatus replica is in the Röntgen Museum in Remscheid-Lennep, Germany. Image taken from Ref. [3].

Attempting to block the path of radiation that caused the glass pane to light up, Röntgen only found lead (Pb) to be sufficient in completely halting the rays. When the physicist held the

Pb up to the pane, he was surprised to see the shape of his hand illuminated on the glass pane. He grabbed photographic paper, which was conventionally used for cameras until this point, and he placed it between his hand and the glass pane, capturing the first x-ray image. The x-rays were found to be still partially passing through the hand, bone included, but the more-dense bone was found to halt *some* of the x-rays, thus showing a distinct illumination of white on black background.

The technology Röntgen mistakenly discovered would become instrumental in the early twentieth century to progress towards modern medicine, as noted in the medical journal by James Taylor, M.R.C.S. [4]. Taylor describes the injury of a young boy's forearm and stated that without the technological assistance provided by x-ray technology, the arm would not have recovered. Instead, it would have likely led to paralysis in the boy's arm. The boy from this journal fully recovered, thanks to a proper diagnosis of the fracture. This diagnosis, as well as many others since the start of the twentieth century, have been a direct result of the work of Wilhelm Röntgen's x-ray discovery. What has become commonplace in an operating room today was only just entering the medical community with unknown precision and little understanding a century ago.

Figure 2. First known medical images of x-ray photography. These images were some of the first captured by x-ray photography, an impactful tool for the medical community. Figure Taken from Ref. [4].

Upon the turn of the twentieth century, the technology of x-rays was studied extensively, as it was just the third discovered component of the electromagnetic spectrum, following the discovery of radio waves just a few years before, and infrared light waves in 1800. As a result, the understanding of the properties of x-rays and their applications was expanded upon vastly in just a few years due to the sheer number of experiments being performed by physicists.

1.1.2. Laue's x-ray Diffraction Discovery

In the early 1900's, the city of Munich was home to many brilliant physicists. The aforementioned Röntgen partnered with Arnold Sommerfeld and Max von Laue to further research the theory of x-rays [5]. One prominent conclusion from the research conducted was the capability of x-rays to diffract. At this point in history, the atomic model theory of J.J. Thomson was generally the working hypothesis employed by physicists, modeled in Figure 3. This model of molecules making up physical solids with discontinuous space between had not yet been supported, though there were plenty of experiments aiming to experimentally verify theory.

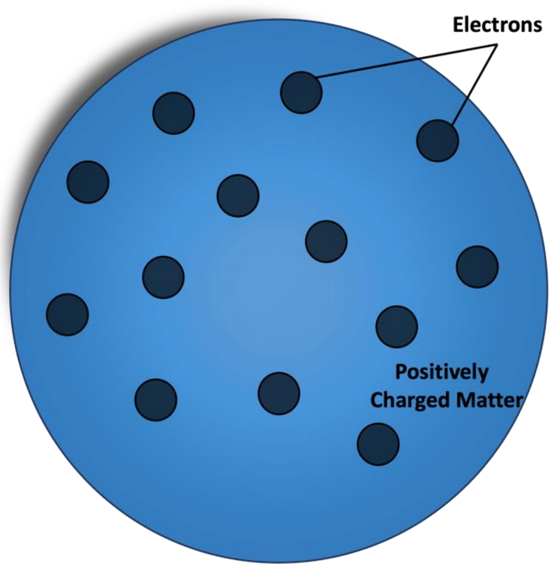

Figure 3. Thomson model of the atom circa 1895. Positively charged matter with minuscule electrons interspersed throughout providing a net charge of 0 of the atom. The model is colloquially called "The Plum Pudding Model" for its appearance. The components of Thomson's model able to be evaluated via x-ray diffraction regarded not their internal makeup but rather the structure of many atoms making up solids.

The research group headed by von Laue aimed to employ this atomic model to predict that a beam of x-rays directed at a sample of copper sulfate would diffract the x-rays. It was believed that x-rays, should they in fact be found to be waves, would possess a wavelength of about 10^{-10} m thanks to the work and subsequent research paper by P.P. Ewald []. Because of the speculative wavelength of the x-rays, Laue believed that the spacing between atoms of a material, a quantity predicted to be smaller than that of x-ray wavelength, would act as a diffraction grating in which a continuous beam of x-rays that passed through the sample would form a pattern on photographic paper beyond the sample. Diffraction of the x-rays would then support the Thomson atomic model hypothesis. Additionally, observation of the x-rays diffracting would allow the two theories to work in tandem to experimentally verify the wavelike nature of x-rays. Results in agreement with the initial hypothesis would look like a large percentage of the incident x-rays on the sample passing through without a change of course, with the rest reflecting off the atoms in a pattern that would be both statistically and optimally geometrically significant. This pattern as depicted in Figure 4 shows the distinct change of course of the wave paths, thus implying diffraction had occurred. While the correct understanding of the composition of the atom wouldn't be discovered for another 11 years by Rutherford, the presence of some diffracted x-rays indicated the existence of dense matter interspersed with space to form solid objects.

Max von Laue then directed two technicians, Walter Friedrich and Paul Knipping, to create and perform such an experiment as Laue had laid out [6]. The instrument that they constructed is currently on display at the Deutsches Museum in Munich and was a rather rudimentary setup comprised of a series of lead screens, a Muller x-ray bulb, the copper sulfate sample, and photographic paper. This experiment can be seen illustrated in Figure 5. The experiment indeed agreed with Laue's theories, and the diffraction of x-rays indicated the wave-like properties of x-rays, giving light to new experimentation utilizing x-rays. The experiment also earned Max von Laue a Nobel Prize [7]. The German Physical Society at the University of Berlin held a meeting on June 8, 1912, where Max von Laue displayed his findings regarding the diffraction of x-rays in crystals, thus attributing wavelike nature to x-rays.

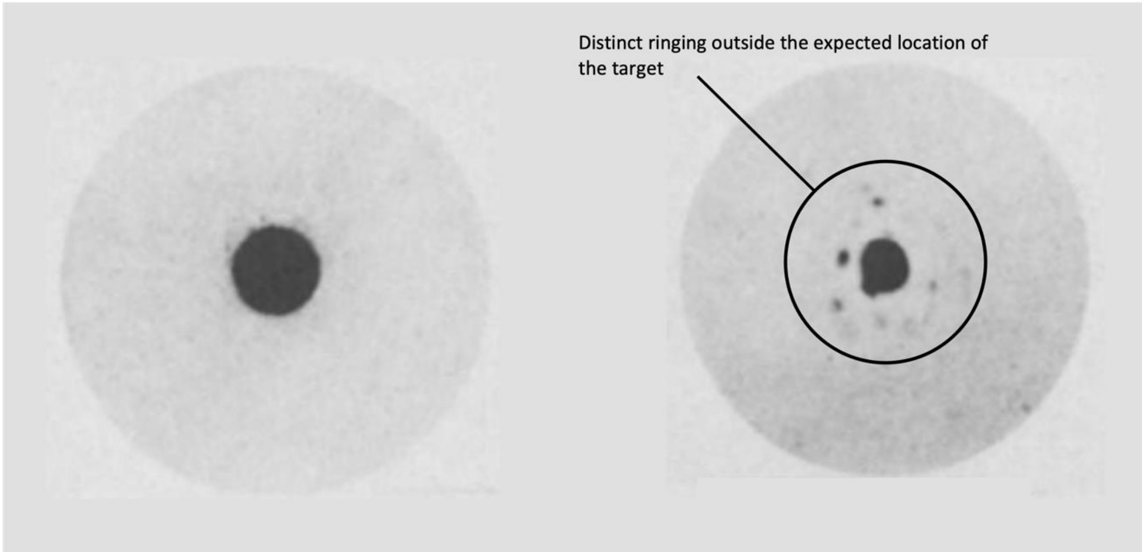

Figure 4. Diffraction patterns of Friedrich and Knipping diffraction experiment. The first image depicts a stream of x-rays in their directed orientation from the target, providing a uniform quantity of x-rays around the center of the imaging paper. The image to the right shows ringing around a much smaller central region of x-rays in which there are clearly x-rays around the intended location of x-rays in the first image. The x-rays in the second image have been diffracted through a copper sulfate crystal, resulting in the ringing of the x-rays further from the central target. Images taken from Ref. [8].

From the time he was a first-year graduate student in university, writing his first paper regarding Laue's research, to his last 10 works at the end of his life, Bragg primarily studied the behavior of waves through crystals. His work regarding crystals focused particularly on their atomic makeup. He utilized the knowledge of x-rays being waves to analyze atomic crystal spacing, finding relative normality throughout samples. Bragg's research also established a foundation for XRD technology and research. W.L Bragg and his father William Henry performed a series of experiments using crystals, namely sodium chloride, zinc sulfide (ZnS, but more typically referred to as zincblende), and diamond, to understand their respective atomic shapes and structures.

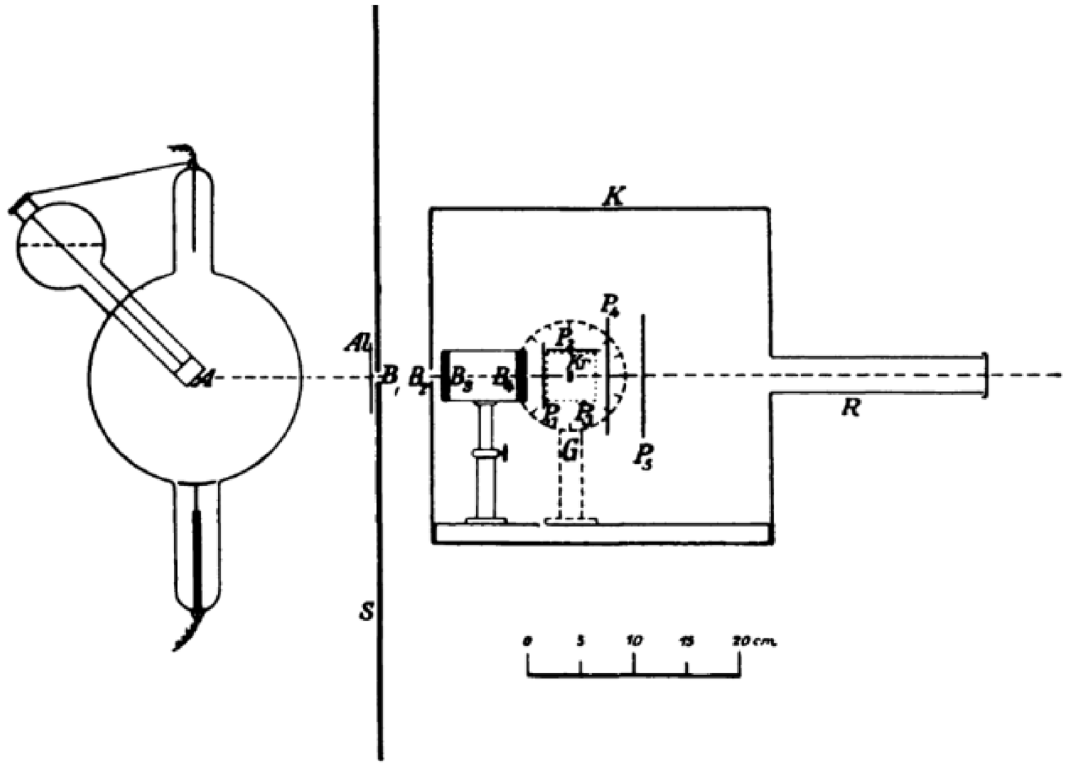

Figure 5. Experimental Apparatus of Friedrich and Knipping Experiment. Similar to Röntgen's x-ray apparatus, a Crooks tube stimulates a cathode to produce x-rays once electrons hit the target. The x-rays were then channeled in the 'K' chamber, focused through collimation tube R, and traveled towards a sample to analyze occurrence of diffraction. Figure taken from Ref. [6].

From the time he was a first-year graduate student in university, writing his first paper regarding Laue's research, to his last 10 works at the end of his life, Bragg primarily studied the behavior of waves through crystals. His work regarding crystals focused particularly on their atomic makeup. He utilized the knowledge of x-rays being waves to analyze atomic crystal spacing, finding relative normality throughout samples. Bragg's research also established a foundation for XRD technology and research. W.L Bragg and his father William Henry performed a series of experiments using crystals, namely sodium chloride, zinc sulfide (ZnS, but more typically referred to as zincblende), and diamond, to understand their respective atomic shapes and structures.

A 1913 article [9] published by the younger Bragg aimed to expand upon the concept of diffraction of the x-rays within a crystal sample. In what would become his most important discovery, Bragg formulated the law that interpreted the constructive interference produced by diffracted x-rays at specific incident angles of a sample. His experiment regarding crystals and their diffraction outputs being trigonometrically dependent on spacing of the atoms between which the x-rays diffract led to the operating theory known as Bragg's Law. Bragg's Law is the mathematically trigonometric relation described by the difference in distance traveled by waves, as Figure 6. Diagram of Bragg's Law illustrates. The law states that the constructive interference created by properly spaced wave separations can reveal the distance of the diffraction grating that some of the waves must have traveled in addition to the distance of the optimized route of the reference wave. Thus, 2a represents the path-length difference traveled between diffracted wave A' and B'. Constructive interference will occur when the d-spacing fits the algebraic function $d = \frac{\lambda}{2 \sin \theta}$ as a result of the phase shift occurring in wavefront B.

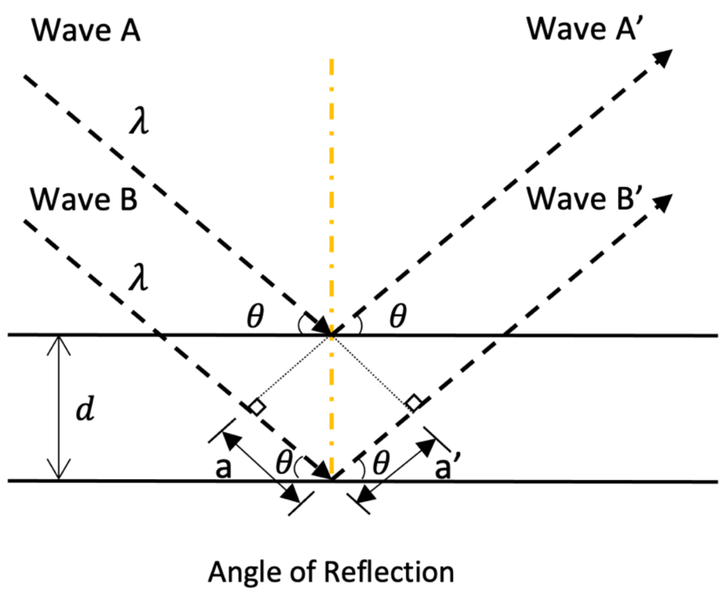

Figure 6. Diagram of Bragg's Law. For two parallel waves A and B incident on two atomic planes spaced d distance away, there is some angle θ that the waves reflect upon such that the 2α phase shift that occurs between the wavefronts produces constructive interference between the two waves.

1.2. Bremsstrahlung Vs. Characteristic X-rays.

There are two ways in which x-rays are produced by electronic interaction within the nucleus. The first of the two x-ray types are known as 'Bremsstrahlung'. Bremsstrahlung x-rays are formed during the process of charged particles accelerating due to external forces. High-energy electrons traveling from a cathode to an anode would be one such example of a system, as seen typically in wave-producing apparatuses. As these electrons travel from the target to a sample, the vast majority will pass near but not collide with nuclei. The attractive force of the nucleus on the electrons will alter the electrons' paths as they travel. In the vast majority of cases the incoming electrons will be 'caught' through electromagnetic attraction to a nucleus and will decelerate drastically. The 'braking' that occurs is where the name of the process came from; "Bremsstrahlung" is German for braking waves. In some cases, an electron will collide with a nucleus, resulting in the transfer of energy from the electron, whose velocity will come to a halt, to a photon emitted during the interaction, in order to adhere to Newton's principles of energy conservation [10].

Bremsstrahlung radiation forms a continuous spectrum of x-rays in relation to angle. Therefore, a crystal with a given plane spacing will diffract Bremsstrahlung radiation at a continuous array of angles, making it unhelpful for crystal analysis. However, the presence of Bremsstrahlung x-rays can be factored out of an x-ray scan because their intensity is smoothly dependent on wavelength. When the high energy electrons coming from the filament reach the target, they can produce an x-ray with energy less than or equal to the energy of the incoming electron. Unless it transfers one hundred percent of its energy to the x-ray, a given incoming electron will continue to travel further into the target and have additional interactions with target atoms. The maximum possible x-ray energy will decrease with each interaction since the energy of the electron is decreasing. As a result, x-ray intensity is zero above the energy of the incoming electrons and increases linearly with decreasing x-ray energy. However, x-ray intensity is attenuated as the x-rays travel out of the source, and lower energy x-rays are attenuated to a greater extent than higher energy x-rays. Therefore, x-ray intensity decreases back to zero at the low end of the energy spectrum. As can be seen in Figure 7 then, the smooth relation between intensity of Bremsstrahlung radiation and x-ray energy will invariably produce a sharper peak of counts at lower intensity, then displaying counts decreasing as a function of increasing intensity after first achieving minimal required energy for the x-rays to begin. Then, due to the continuous spectrum of Bremsstrahlung x-rays as a function of wavelength, their anticipated output can be accounted for and functionally extracted such that the discreet peaks produced by characteristic x-rays are most prominent.

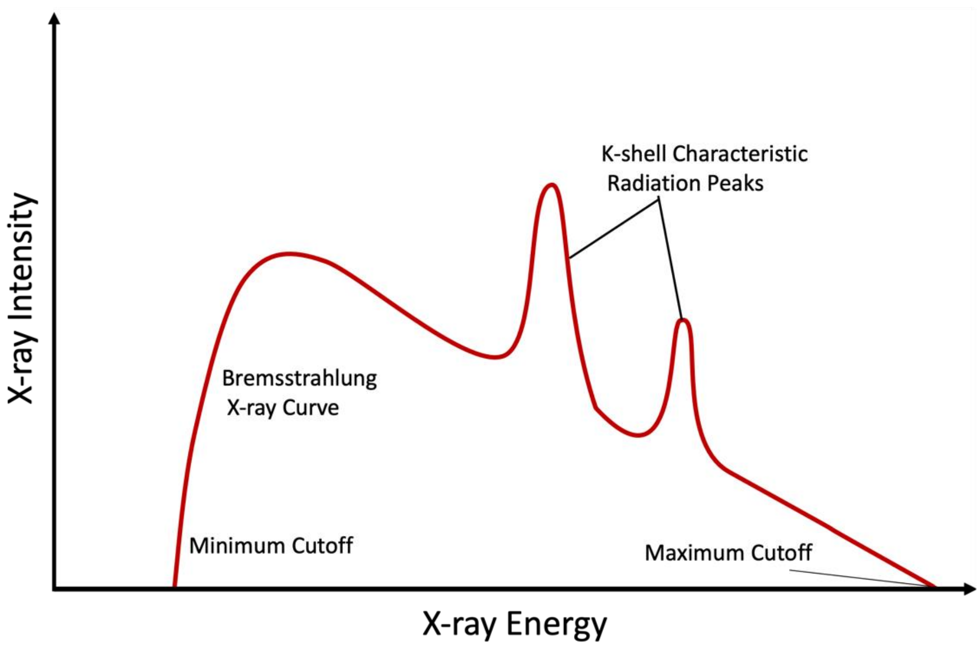

Figure 7. Bremsstrahlung curves via incident electron intensity and wavelength. The Bremsstrahlung curve is consistently seen in spectroscopies utilizing x-rays. The shape of the curve corresponds to the intensity of the incident electrons relative to the incident energy the electrons are projected at. K-shell x-rays, where characteristic x-rays are produced as a result of electrons displaced from the k-electron shell, are most typically seen in x-ray spectroscopy as a result of their high energy level compared to other shell electron interactions. Characteristic x-ray peaks widened on x-axis for effect.

The second variation of x-ray is called 'characteristic'. Characteristic x-rays are produced through the interaction of high-energy electromagnetic radiation or charged particles with the atoms of the target. The process begins with the incident radiation, which carries sufficient energy to interact with the electrons within the atoms of the target material, as described in Figure 8. When an incident particle transfers enough energy to eject an inner-shell electron, this creates a vacancy within one of the atom's inner electron shells, leaving the atom in an excited state. To stabilize itself, an electron from a higher energy level or outer shell of the atom transitions to fill the vacancy created in the inner shell. This transition releases energy in the form of an x-ray photon. The energy of this emitted x-ray photon corresponds to the energy difference between the initial and final energy levels of the electron transition, which is characteristic of the specific element and the energy levels involved in the transition.

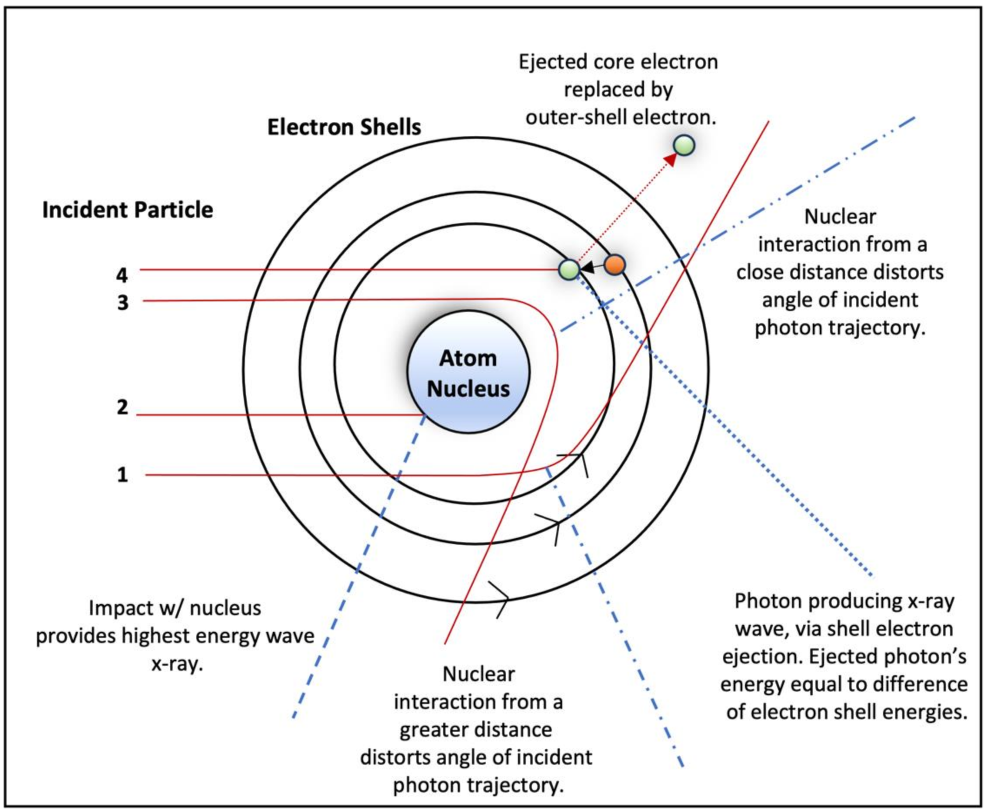

Figure 8. Electron interactions around the nucleus. Characteristic and Bremsstrahlung x-ray production via multiple incident particle interactions, with four possible outcomes dependently on interaction. Electrons 1-3 display various forms of Bremsstrahlung x-ray production. Incident electron 1 shows the electron succumbing to weak nuclear interaction and therefore changes path due to the radial force. Electron 2 directly collides with the atoms' nucleus and comes to a stop thus transferring all its kinetic energy in the emission of a photon. The third electron underwent change in path due to attraction close to the nucleus of the atom, but in comparison to electron 1, electron 3 was on a trajectory far closer to the nucleus, and its path skews far more than the former. Incident particle 4 displays the process in which characteristic x-rays are produced. The energy of the x-ray photon via the shell-electron and incident electron collision is determined by the energy level difference the shell-electron falls from outer shell to inner shell.

While all x-rays will diffract by Bragg's Law, only characteristic x-rays will diffract in ways that produce discreet peaks in relation to incident angle. Thus, these characteristic x-rays are of primary interest to the effect of physical analysis.

1.3. X-ray Diffractometers

1.3.1. XRD Functionality

Upon the discovery of x-rays showing characteristics of waves, the scientific world was set alight with experimenting, using the relatively accessible x-ray. Not only were x-rays reliable to produce, but they behaved in calculable and expected patterns. After the discovery of diffracting x-rays through apertures between patterned atomic spacing, the x-ray was seen as the primary tool of experimentation when dealing with quantum spacing (<10 nm). By stimulating electrons to produce high-energy waves to analyze quantum spaces with precision due to the relative wavelengths of x-rays being the same magnitude, one can utilize Bragg's Law to find ranges of incident angles that produce high constructive interference.

1.3.2. History of Early XRD

The first XRD began experimentation with rudimentary setups purely to observe the diffraction of x-rays at angles expected by the law of reflected waves. The Bragg father and son duo assembled their instrument in 1912 [11]. This XRD possessed the capability to form spectroscopies of rudimentary quality, with lots of uncertainty. Over the next decade their results increased in reproducibility and were experimentally verified. As the research was presented to the public sector, the Bragg x-ray work, based on the fundamental concepts previously established by Thomson, opened the eyes to scientists from abundant fields regarding the potential applications these waves possessed.

As a result of the reliability of x-ray production and analysis, articles of small or unknown size could be examined. One of the most prominent discoveries found by the utilization of XRD was the famous Watson and Crick paper on the back of the Rosalind Franklin experiment: the structure of DNA [12]. The image produced from XRD basing the theorized shape of DNA strand structure, commonly referred to as 'Photo 51' is illustrated in Figure 9. Without the XRD spectroscopy, the subsequent research papers would have been far less empirically argued.

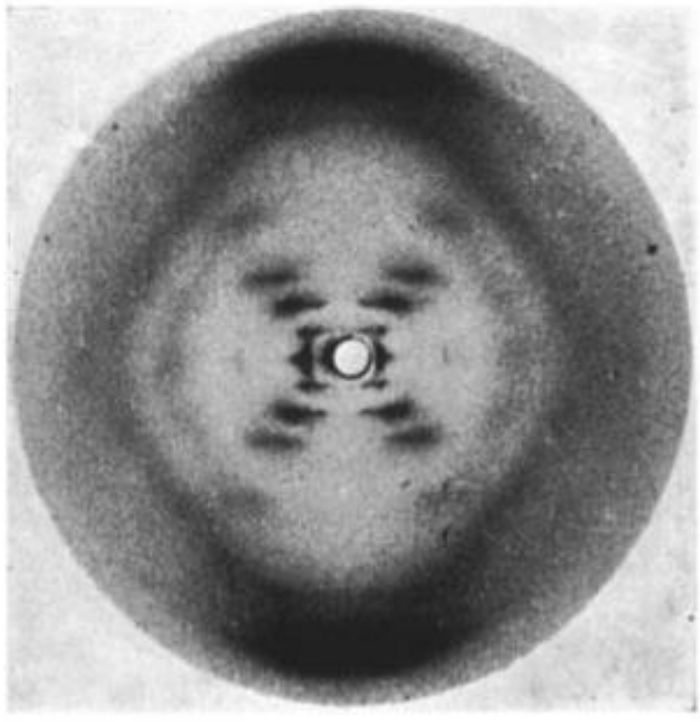

Figure 9. XRD results of the Watson and Crick experiment. As a result of the XRD imaging found by Rosalind Franklin, Photo 51 depicts distinct double helix shaped patterns of phosphate structures, DNA structure was identified for the first time. This 1952 experiment unfolded the helical DNA strands and found the spacing between the two structures as a result of their diffraction patterns. Figure taken from Ref. [13].

A vast modern field using the diffractometry approach is the applications of XRD as a quality control tool in electronics. One such class within the field is the study of thin films. Thin films are materials that are layered upon each atomic level to form substances of thicknesses from nanometers to a micrometer, with larger lengths and widths in wafer shapes. While the scope of their applications are still unrealized, thin films are highly versatile in electronic manufacturing.

1.4. Thin Films

1.4.1. Lattice Structures

Lattice structures refer to the three-dimensional shape of the unit cell, the most basic orientation of atoms that materials tend to orient themselves into. The unit cell is a geometrically consistent orientation of the atoms, repeatedly stacked upon each other to 'build' the element or compound together. The unit cells are of constant interatomic spacing apart and the atoms within the unit cell are orientated uniformly, with that distance being dependent and unique to each chemical compound. Of the 14 total lattice structures found, there are primarily four types of lattice structure orientations for metals: simple cubic (SC), body-centered cubic (BCC), hexagonal tightly packed (HCP), and face-centered cubic orientations (FCC). Figure 10 displays the FCC lattice structure in a 'cubic' orientation, along with an orientation that places the molecules along vertically equidistant spacing. These orientation types have set quantities of atoms to a structure. In general, the lattice structures will tend to orient themselves such that uniform distance between atoms are established.

Given that each element has a unique place spacing, it would follow then that XRD could discern elements via their lattice spacing. The lattices of substances work as diffraction gratings for x-rays, allowing XRD to ascertain the spacing between atom layers. As a result of the consistency of x-rays as a tool for measurement was realized, XRD research led by Bragg as well as many other scientists at the time, began their research on the spacing of elements around 1920.

About a decade after the discovery of the consistency of the unit cell of individual elements, the next big discovery regarding the cellular structure of compounds was by W. A. Wood in 1931 [14]. Wood discovered that cold-drawing constantan wire would distort the shape of the unit cell lattice structure. The act of cold drawing is a process in which wire or metal is both elongated and compressed along the central axis of the wire, depicted in Figure 11. Cold-Drawing Constantan wire cross section The result is a wire with a more uniform and smoother finish. As was additionally discovered, the wires possessed increased mechanical properties due to their reconfigured atomic structure. These mechanical properties coincided with an increase in uniform dimensional tolerance due to the process, resulting in wire that was consistent in size with stronger properties.

However, a byproduct of the cold-drawing process is that the compound lattice structure shape undergoes a degree of distortion. Wood was the first to discover this change in lattice structure, though many had theorized this concept and performed experiments to test its validity. Wood described the distortion to the shape via the result of measuring the diffracted x-rays before and after undergoing the process.

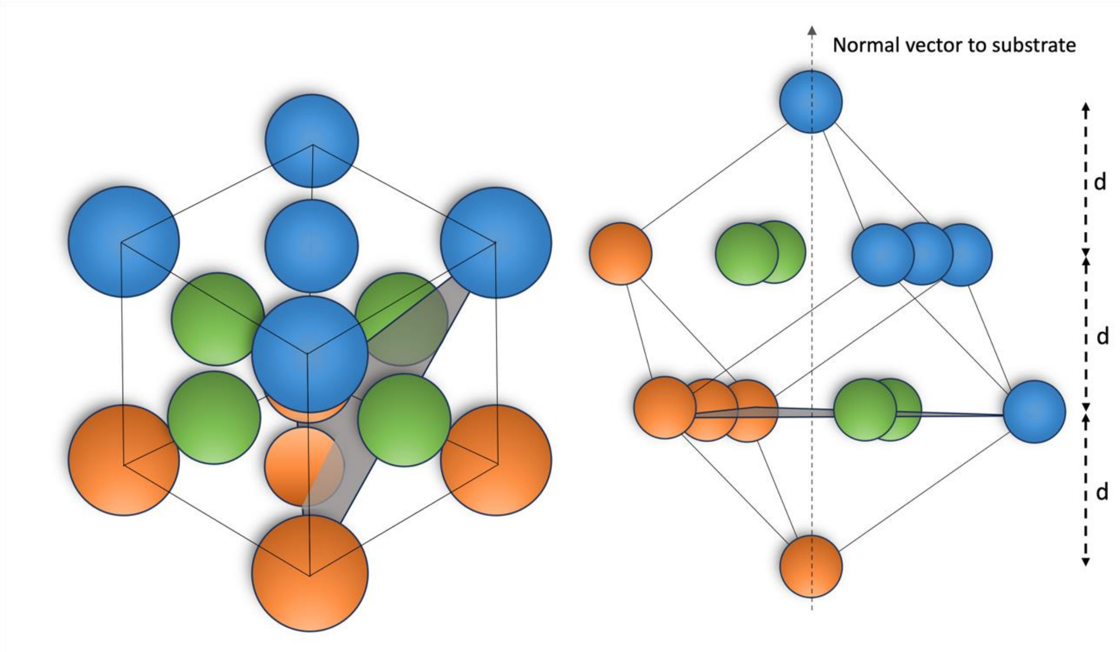

Figure 10. Diagram of Face-Centered-Cubic (FCC) lattice structure. The left image displays the most common orientation of atomic placement in isometric view. The right image displays a scaled up and rotated view of the image prioritizing the spacing between atomic layers as deposited. This orientation will be layered normal to the substrate of a thin film, and the distance *d* will be distinguished between atomic spaces for all lattice structures placed in tandem. The atomic plane spacing establishes 'layers' for x-ray reflection to occur against, which can then determine angles of incident x-rays in which large quantities of x-rays will diffract, using Bragg's law. The reference plane consistent in both images displays one layer of atoms parallel to the substrate.

The research operated on the grounds of Bragg's research and corresponding theory, that crystal structure is fixed in place. This distortion that Wood described as a result of cold drawing differed from the change in size to the orientation of atoms but presented more a change in shape to the constantan lattice or change to the interatomic spacing through the chemical and mechanical processes performed on the wire.

The discovery of distortion to crystal structure was monumental, achieved using XRDs to quantitatively determine the change in structure. This was particularly important because it offered a new idea of the cellular structure of materials being less "fixed" than previously notioned.

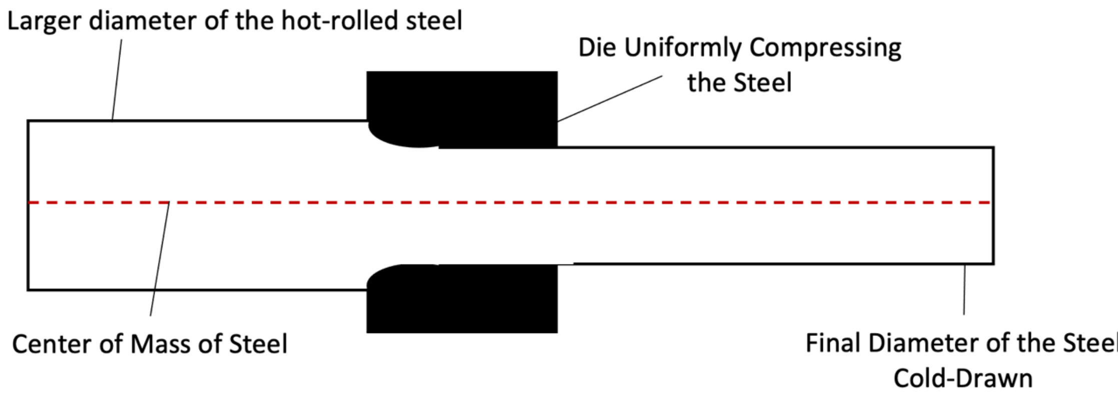

Figure 11. Cold-Drawing Constantan wire cross section. In this figure, the cross section shows the Carbide undergoing the process, which will change the lattice structure shape and size of the Carbide. Uniform compression through the die along with rapid cooling of the steel to adjust the crystalline structure of the wire. This process was one of the first indications of mechanical changes to lattice structure. The process has since been used to manipulate and optimize the mechanical functions of certain metals, most often used in wires.

Thin films themselves were initially constructed with the intention of studying optics in the 1800's. Michael Faraday's 1832 presentation and subsequent write-up delved into the creation of glass charging tubes to evaluate the optics of electric discharges [15]. Faraday described brass electrodes used within the glass charging tubes which would have been constructed via deposition of brass in thin film form. While the thin films created were a byproduct to serve a purpose of a greater experiment, the utilization of thin films in this instance drew Faraday to multiple conclusions regarding the behavior of electricity and magnets. As technological innovations over the 19th, 20th, and 21st centuries led to electronics that shrank in physical size, the utilizations of thin films in circuitry became more commonplace.

1.4.2. Thin Film Application

The importance of thin films and their research is based upon the concept of optimization. To maximize the thin films physical properties to their full potential, it is essential to first gain a proper understanding of the structural composition of thin films. For instance, the process of annealing tools with thin metallic polymers can contribute to their overall strength and durability. This process of annealing polymers onto tools coats the tools with the element or compound of desire and hardens onto the tools in a thin coat. Polymer annealing is often seen in electronics to promote congruency of circuitry, and aids in material ductility of the electronics themselves. Thin films can also be useful in cases where materials are expensive or impractical to acquire. In such a case, a thin film can be used to coat another material while maintaining the physical and atomic structural properties of the film. In other cases, the films can be used for their versatility as light-weight metals with electronic capability.

The research of thin films is consistently researched and developed currently. The configurations of alloys deposited onto substrates are numerous and can offer different benefits depending on the conditions of need. There is also need for thin film analysis regarding the structure of atomic layers for electrodynamic systems, where electric paths and circuitry are etched into the thin films. Etching for electric processes especially requires uniform and expected lattice patterns throughout the entirety of the thin films. Misalignment or error of shape of any atomic layers will cause deformities in the thin film, and etchings will pose a threat to breakage of the film, especially when current flows through the deformity. Thus, thin film analysis requires high precision, which can only be offered by a piece of machinery with a low degree of error and high degree of measurement capability. The x-ray diffractometer poses as such a machine.

The latest in thin film technology has been seen in their utilization in flexible photovoltaic solar panels. One noteworthy example was Tesla Inc.'s recent public partnership with Hanergy Thin Films in production of solar power cells for Tesla car chargers [16]. In this case, the solar panels are constructed with copper indium gallium selenide (CIGS) thin films that boast the highest found energy conversion in solar panels with 21%. The thin films Hanergy has acquired through subsidiary patent [17] were developed to limit the long-term depreciation of the panels from sun damage. To verify the consistency of their thin film technology both throughout an entire cell and across production and distribution, their films would be tested of structural uniformity by XRD.

1.4.3. Thin Film Creation

Thin films are typically created by the deposition of the material of the film onto a substrate. There are two main categories of thin film deposition, called chemical vapor deposition and physical vapor deposition respectively. Chemical Vapor Deposition (CVD) utilizes a chamber brought to low pressures where gas is pumped in and ionized. The ionized gas is then attracted to a negatively charged field where a substrate containing the desired sample material is located. The gas is then accelerated towards a negatively charged well where a substrate is located. The gas that embeds itself on the substrate is cooled and a physically solid thin film is coated onto the substrate.

Physical Vapor Deposition (PVD) differs from CVD in the fact that the desired sample material is in a liquid or solid state in PVD. One form of PVD is called sputtering, which tends to be the most common type of thin film deposition. In this process, again ionized gas is used to bombard a crucible. The gas particles are accelerated towards the crucible, bombarding the desired material with atomic collisions, manifesting energy transfers into the sample material. The particles from the desired material then travel throughout the entirety of the pressurized chamber, and some deposit themselves on the substrate. There are a few other techniques making up the PVD method of deposition, including the Thermal Forming Process, Electro-Processes and Mechanical techniques, with each process having its advantages and disadvantages. Sputtering however, tends to be a common method of deposition for its low cost relative to other chamber designs.

After deposition has occurred in either of the PVD or CVD methods, the annealing process begins. During annealing, the particles that have been deposited will form grains, or small clusters of lattice structure orientations in consistent atomic structuring and patterned sequences amidst the thin film. These grains that are formed are numerous, but during the annealing process, some grains will overgrow the grains around it, resulting in fewer total grains, of varying size and orientation. The quantity of grains and their various orientations on thin films is one of the main properties of that film that determines the resistance, the flexibility, and the ability to undergo stress; each of these components being able to be manipulated to serve a purpose in the technology it is a part of. Small grain structure in the film would indicate a higher stress the film can undergo. Similarly, a smaller lattice structure, or tighter regular interatomic distance, would indicate higher rigidity and ability to be etched for a thin film. Consistent lattice structure will increase flexibility of the thin films and etching ability.

The production and analysis of thin films offer opportunities for further discovery in the factors that may cause impurities during thin film deposition. Not only do thin films have many applications in which the mechanical properties, and specifically grain analysis, are fundamental to the capability and efficiency of thin film performance; an in-depth analysis of the grain structure of a thin film can be the difference between a cell phone's lifetime being a month and multiple years. A spectroscopy of a thin film can illustrate the grain structure and orientation of the sample, simply by analysis of the points of constructive interference and their angles of incident waves on various locations of the thin film.

1.4.4. Structure Inconsistency in Thin Films

During the annealing process of thin film production, there has been a regular occurrence in which the size of grains will increase, and consequently, number of grains in the film may alter. For some applications of thin films, it is optimal to have as consistent grain orientation throughout the film as possible. As annealing of thin films occurs, transitions from one lattice orientation to another will occur as crystal grains grow and compete for space. As a result, the intended orientation of the cross-sectional cubic plane that deposits will be inconsistent, regardless of method of deposition and annealing. Baker, Hoffman et. al discussed the potential ways to find consistency throughout a thin film, suggesting various film thickness and annealing temperature could be dependent factors in percentage of consistent grain orientation present in a sample [18]. The group found that the reasons that these grain growths occur relates to the minimization of potential energy of the lattice structure orientations when forming during annealing, but a method to reproducibly eliminate large grain growth has not been formulated. The research group tested multiple hypotheses on the grounds of combinations of annealing temperature, film thickness, and time of deposition, and found that there are critical annealing temperatures that produce more grain growth inconsistency by percentage of the film's surface. Then, if one orientation of thin film is desired, like for example the uniform atomic spacing normal to the substrate depicted in Figure 10, determining ideal annealing temperatures, time of deposition, and film thickness is necessary. Further research into the optimization of structural consistency could aid in overall quality of the physical and electrical systems they are a part of.

1.5. Houghton University XRD

Houghton University previously worked in collaboration with Cornell University on an extended thin film production research program. Most summers since 2007, Summer Research Institute (SRI) groups traveled to Cornell to work on the analysis of the thin films produced there. Much of the analysis was performed using the Cornell XRD in their facility. The project of undertaking a thin film production and analysis laboratory at Houghton University allowed physics majors and summer research teams to produce thin films on campus.

To construct thin films at Houghton University, thermionic emission was utilized in a deposition chamber. This form of PVD, similar to sputtering, offers a low-cost method of producing thin films. It differs, however in the method of electron stimulation and emission. Rather than ionized gas bombarding the material, an electron gun is used to stimulate the material until evaporation. During thermionic emission a filament is stimulated by large flowing current, and electrons are emitted due to the exceedingly high temperatures reached in the filament. There has been recent success with the deposition chamber in producing thin silver films onto substrates of varying material and desired thickness. Due to the exceptionally low pressures and simultaneously high voltages required in thermionic emission, operation and developmental complications have hindered progress, as mentioned by Jared M. Malone in his thesis on the Houghton Deposition chamber [19]. However, the deposition chamber instrument has also approached readiness and ability to produce thin films consistently.

The XRD at Houghton University was constructed specifically for the use of thin film analysis. The project has been underway since 2010 and has been passed from one graduating student to the next underclassman on 5 different occasions since its beginning. The use of an x-ray Diffractometer to analyze the grain structure and orientation of thin films will become necessary if Houghton University is to produce thin films. Diffractometry, along with an intensive study into the stress-taking abilities of thin films could aid in determining important mechanical and electronic properties of thin films. Upon the arrival of thin silver films at Houghton University via the deposition chamber, the films would be able to be studied with the XRD. Then, extensive independent research on primarily thin silver films could be produced here at Houghton University.

The Houghton XRD is a Bragg-Brentano theta-2theta type orientation and makes use of two rotating arms connected on a fixed central axis. One axis holds the sample mount, centered in front of the x-ray source and its collimating pipe. The other arm holds a steel box-encased radiation monitor. The monitor is a Geiger meter which connects to a Vernier LoggerPro program interface unit, measuring the number of radiation counts over a given time interval.

Thus far, the Houghton XRD has produced two true diffraction spectroscopies depicting peaks. The latest peak to be found was taken in 2021 and is discussed in Section 4.1. The only other true Bragg peaks to have been found before belongs to Heather Phillips, found in 2017 using a silicon wafer sample during her thesis research [20]. Her scan depicted the results of particularly x-rays from 59 to 79 degrees to emphasize the peak found at 69 degrees illustrated in Figure 12. The peak determined the sample's lattice spacing in agreement with the known Bragg angles of Silicon.

More scans are planned to be taken throughout the next semester and the coming years. The primary goal of the research conducted for the purpose of this thesis was to reduce some of the error involved with XRD measurement, to make some mechanical substitutions and enhancements, and to make fixes in the circuitry to both avoid long-term breakage of electrical components and to optimize consistent power and current to the electronics.

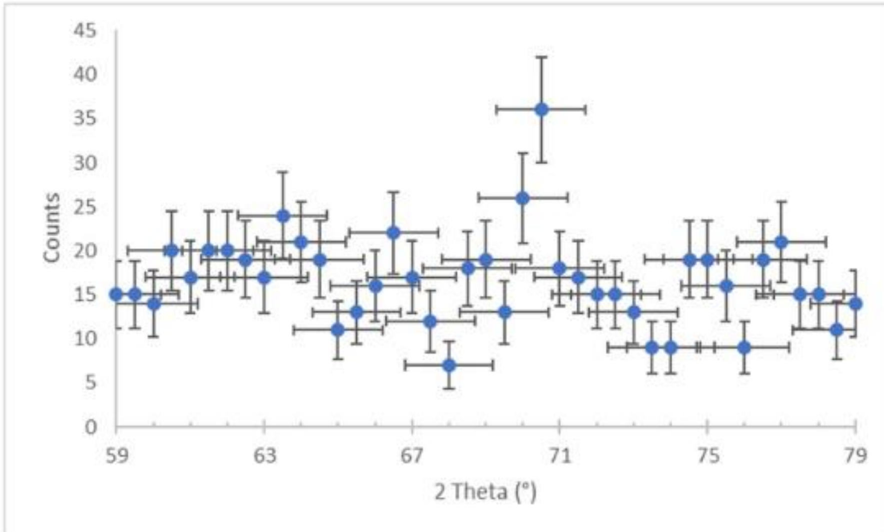

Figure 12. Heather Phillips Houghton XRD Scan. The first XRD scan displays a Bragg angle peak at the 2-Theta 70.2° angle. The 2017 scan used a Silicon sample with a peak of about 40 counts, and almost twice its background radiation counts.

2.1. Wave Energy

2.1.1. Constructive Interference of Electromagnetic Waves

In order to determine constructive wave interference, electromagnetic wave energy must first be derived. The derivation begins with the utilization of Maxwell's four equations of electromagnetism [21]:

$$\vec{\nabla} \cdot \vec{E} = 0\,, \qquad \vec{\nabla} \cdot \vec{B} = 0,$$
$$\vec{\nabla} \times \vec{B} = \mu_0 \varepsilon_0 \frac{\partial \vec{E}}{\partial t}, \quad \text{and} \quad \vec{\nabla} \times \vec{E} = -\frac{\partial \vec{B}}{\partial t}. \tag{1}$$

Suppose an electric field exists solely in the y direction, and a magnetic field exists solely in the z direction, varying along the x-axis. Then, when taking the curl of said E-field, the following will be produced;

$$\vec{\nabla} \times \vec{\mathrm{E}}(\mathrm{x,t})\,\hat{\jmath} = \begin{vmatrix} \hat{\imath} & \hat{\jmath} & \hat{\mathrm{k}} \\ \dfrac{\partial}{\partial x} & \dfrac{\partial}{\partial y} & \dfrac{\partial}{\partial z} \\ 0 & \mathrm{E(x,t)} & 0 \end{vmatrix} = \frac{\partial \mathrm{E}(x,t)}{\partial x}\hat{\mathrm{k}}. \tag{2}$$

Then, setting this cross-product's magnitude equal to its magnetic field equivalent via Maxwell's Equations in Equation (1), the result gives a time-space dependence between the electric field and magnetic field, respectively, as shown

$$\frac{\partial \mathrm{E}(x,t)}{\partial x}\hat{\mathrm{k}} = -\frac{\partial \vec{\mathrm{B}}(x,t)}{\partial t}. \tag{3}$$

Notice that only the magnitude is considered. Continuing the same process with the magnetic field, its curl yields

$$\vec{\nabla} \times \mathrm{B(x,t)}\,\hat{\mathrm{k}} = \begin{vmatrix} \hat{\imath} & \hat{\jmath} & \hat{\mathrm{k}} \\ \dfrac{\partial}{\partial x} & \dfrac{\partial}{\partial y} & \dfrac{\partial}{\partial z} \\ 0 & 0 & \mathrm{B(x,t)} \end{vmatrix} = -\frac{\partial \mathrm{B(x,t)}}{\partial x}\hat{\jmath}. \tag{4}$$

Again equating the value to the Maxwell equation via the output of the curl of the B-field's magnitude,

$$\frac{\partial B(x,t)}{\partial x}\hat{\jmath} = -\mu_0\varepsilon_0\frac{\partial \vec{E}(\mathrm{x},t)}{\partial t}. \tag{5}$$

Thus, the spatial component of the magnetic field has a time-dependent electric field component attached to it. As also shown above by Equation (3), there is a time-dependent magnetic field as a result of a spatial electric field as well. If the partial derivative of Equation (3 is then taken with respect to x,

$$\frac{\partial}{\partial x}\frac{\partial \mathrm{E}}{\partial x} = -\frac{\partial}{\partial x}\frac{\partial \mathrm{B}}{\partial t} \rightarrow \quad \frac{\partial^2 E}{\partial x^2} = -\frac{\partial}{\partial t}\frac{\partial B}{\partial x}, \tag{6}$$

we can replace the $\frac{\partial B}{\partial x}$ quantity with its equivalence from Equation (5,

$$\frac{\partial^2 E}{\partial x^2} = -\frac{\partial}{\partial t}\frac{\partial B}{\partial x} = -\frac{\partial}{\partial t}\left(-\mu_0\varepsilon_0\frac{\partial E}{\partial t}\right) = \mu_0\varepsilon_0\frac{\partial^2 E}{\partial t^2}. \tag{7}$$

Then, the time and space dependent electric field equation

$$\frac{\partial^2 E}{\partial x^2} = \mu_0\varepsilon_0\frac{\partial^2 E}{\partial t^2}, \tag{8}$$

can be characterized by the second order differential equation. Similar steps can be taken to also show the space and time dependent differential equation of the magnetic field,

$$\frac{\partial^2 B}{\partial x^2} = \mu_0\varepsilon_0\frac{\partial^2 B}{\partial t^2}. \tag{9}$$

Then, one solution to the differential equations for both magnetic and electric fields would be characteristic sinusoidal wave equations,

$$\mathrm{E} = \mathrm{E}_0\sin(k\mathrm{x} - \omega\mathrm{t} + \phi) \text{ and } \mathrm{B} = \mathrm{B}_0\sin(k\mathrm{x} - \omega\mathrm{t} + \phi), \tag{10}$$

where k is the wave number, and ω is the angular frequency, with a general phase shift of the equation, ϕ, in the offset wave from its system.

For electromagnetic waves traveling in a vacuum, both Equations (8) and (9) can be solved by one-dimensional waves if the constants

$$\mu_0\varepsilon_0 = \frac{1}{c^2}. \tag{11}$$

Then, the two simple sinusoidal wave equations can be placed into the relation established in Equation (3;

$$\frac{\partial}{\partial x}\left(\mathrm{E_0}\sin(k\mathrm{x}-\omega\mathrm{t}+\ \phi)\right)=-\frac{\partial}{\partial t}\left(\mathrm{B_0}\sin(k\mathrm{x}-\omega\mathrm{t}+\ \phi)\right), \tag{12}$$

and the partial derivatives are

$$-\mathrm{kE_0}\sin(k\mathrm{x}-\omega\mathrm{t}+\ \phi)=-\omega\mathrm{B_0}\sin(k\mathrm{x}-\omega\mathrm{t}+\ \phi),$$

then

$$\mathrm{E_0}=\frac{\omega}{k}\mathrm{B_0}\ , \tag{13}$$

as all other terms cancel. Since $\omega = 2\pi\mathrm{f}$, where f is the wave frequency, and $\mathrm{k}=\frac{2\pi}{\lambda}$, the relation can be stated where

$$\frac{\omega}{\mathrm{k}}=\lambda\mathrm{f}=\mathrm{c}, \tag{14}$$

the speed of light in a vacuum. Thus, the amplitudes of the magnetic field and electric fields are directly proportional, described by the equation

$$c=\frac{\mathrm{E_0}}{\mathrm{B_0}}, \tag{15}$$

where $\mathrm{E_0}$ and $\mathrm{B_0}$ represent the maximal amplitudes of the electric and magnetic fields, respectively. Then, the ratio of the electric field to the magnetic field in an electromagnetic wave will always equal c. As displayed in Equation (13, one solution to the electric field differential equation can then describe the x-rays produced via an x-ray tube:

$$\mathrm{E}=\mathrm{E_0}\sin(k\mathrm{x}-\omega\mathrm{t}+\phi). \tag{16}$$

Let us propose the presence of two identical wave equations representing the paths of released photons.

$$\mathrm{E_1}=\mathrm{E_0}\sin(\mathrm{kx}-\omega\mathrm{t}+\varphi),\qquad \text{and}\qquad \mathrm{E_2}=\mathrm{E_0}\sin(\mathrm{kx}-\omega\mathrm{t}). \tag{17}$$

Here, These waves have equal amplitudes, waveforms, and angular frequency. Their only difference is represented by a relative phase shift, though their trajectories are parallel, incident upon a surface. Then, the superposition principle states that the addition of those two waves in Equation (17 will have the combined amplitude of the two waves, as described by

$$\mathrm{E_p} = 2\mathrm{E_0}\cos\left(\frac{\varphi}{2}\right)\sin\left(kx - \omega t + \frac{\varphi}{2}\right). \tag{18}$$

Thus, the amplitude of the superposition of the wave equation for the two photons that produce the x-rays is dependent on a specific part of the equation, the cosine term.

The amplitude of the constructive interference can be rescaled under the conceptualization of a plane wave produced by an XRD. It is then demonstrated that the amplitude is maximized when the cosine terms is equal either to 1 or -1. Furthermore, a negation of the amplitude can simply be rewritten as a phase shift of the entire wave equation by 180 °, but the magnitude would remain the same. Then, the amplitude of the peaks of the wave equations, Equation (18, can be rewritten such that

$$\mathrm{A} = \left|2\mathrm{E_0}\cos\left(\frac{\varphi}{2}\right)\right|. \tag{19}$$

Conceptually, the phase shift of such a wave will relate to the change of its wavefront position, denoted by

$$\varphi = \mathrm{k}\Delta\mathrm{x}, \tag{20}$$

where Δx is the path-length difference between $\mathrm{E_1}$ and $\mathrm{E_2}$.To maximize the amplitude, the phase shift must be a multiple of 2π.

Therefore,

$$\Delta\mathrm{x} = \frac{2\pi\mathrm{n}}{\mathrm{k}}, \tag{21}$$

where n is an integer indexing the multiplicity of wavelength

$$\frac{2\pi}{\mathrm{k}} = \lambda, \tag{22}$$

and thus, the distance between waves to achieve maximum amplitude is given by integer multiples of the relation established in Equation (19), nλ. At these distances between wavefronts, constructive interference will be at its greatest. Thus, maximal amplitude will adhere to the equation

$$A_{max} = 2E_0 \cos\left(\frac{n\lambda}{2}\right). \tag{23}$$

2.1.2. Poynting Vector and X-ray Intensity

Additionally, the intensity of an x-ray wave can be derived via the Poynting vector, or

$$\vec{S} = \frac{1}{\mu_0}\vec{E} \times \vec{B}, \tag{24}$$

where S describes the rate at which energy passes perpendicular to the cross-sectional area described by the electric and magnetic field. Given that the electric field and the magnetic field are perpendicular to each other,

$$S = \frac{1}{\mu_0}EB = \frac{1}{\mu_0}\frac{E^2}{c}, \tag{25}$$

when also considering equivalence of B in Equation (15. Then, intensity of an electromagnetic wave is denoted as

$$I = S_{avg} = \frac{{B_0}^2}{2\mu_0 c} = \frac{{E_0}^2}{2\mu_0 c}. \tag{26}$$

Equation (26) represents intensity in both components of magnetic field and electric field. As a result, intensity can be written in terms of wave amplitude, thus leading to the conclusion that x-ray intensity and the square of the amplitude are proportional.

2.2. Bragg's Law

Given that a path length difference is necessary to create constructive interference between two waves of equal incident angle, the spacing in which the second wave travels to reflect against can be manipulated. As was described in Equation (23), the maximal amplitude will occur when the path length difference between the two waves is an integer multiple of wavelength. Then,

$$\Delta x_{\text{max Amplitude}} = n\lambda, \tag{27}$$

and the resulting path length difference can be found via the geometric relation described in Figure 13. Bragg's Law Diagram and Geometry

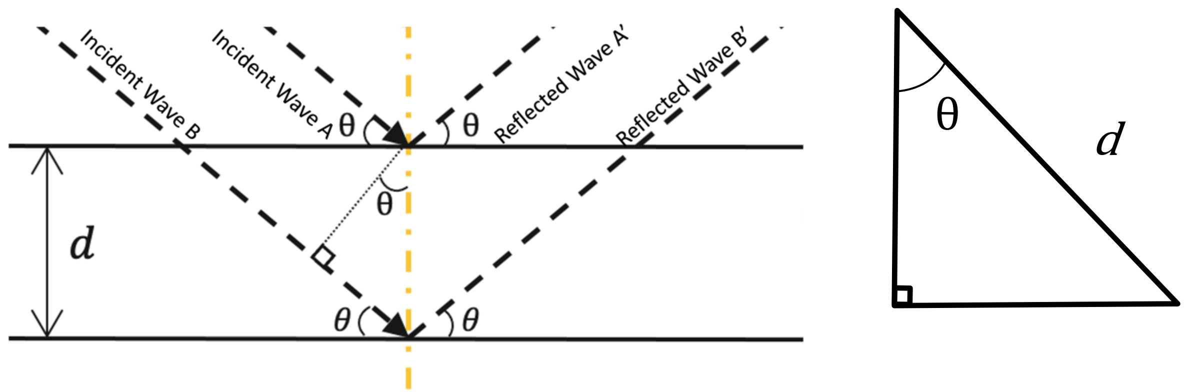

Figure 13. Bragg's Law Diagram and Geometry. The triangle formed by the angle of reflection, the incident x-ray and trigonometric angle identity, and the segment attaching the point of Wave A's reflection and a point perpendicular to Wave B gives the path-length difference traveled by the wave to the point of reflection the function $\ell = \mathrm{d}\sin(\theta)$. After reflection, the wave travels an additional ℓ for a total path-length difference of $2\mathrm{d}\sin(\theta)$.

In this method, measuring the lattice structures of crystals or thin films by their atomic spacing is possible using XRDs. The law is thus denoted by the equation

$$n\lambda = 2d\sin(\theta), \tag{28}$$

where n is an integer, and d is multiplied by $2\sin(\theta)$, due to the path length-difference traveled by the longer traveling x-ray, changing the phase shift of B' such that the waves are once again in phase. Constructive interference is measured at these such integer multiples of the wavelength of the x-rays.

When more than 2 waves produce constructive interference within the context of XRD, the respective phase shifts of each wave will have to offset each other such that their coincidence, Δx, aligns to maintain parallelism when reflected off the sample. Because destructive interference naturally also exists where constructive interference may be present, the general phase shift and alignment of waves becomes necessarily more precise to produce any form of constructive interference as more waves are added to a system. If, for a given set of N planes, there exists a pair of planes separated by md (where m is an integer much less than N) that result in destructive interference, then the diffraction from the set of N planes will in general be destructive. Additionally, the angle of first order (n=1) destructive interference decreases as m increases. Therefore, the angular width of generally constructive interference decreases as N increases. Then, for Bragg angle peaks to occur, hundreds of waves must align in integer multiples of the x-ray energy to produce constructive interference, which will look like distinguishable quantities of x-ray counts in very thin peaks.

Equation 20 is of utmost importance to ascertaining the spacing of the lattice structure of the sample of measurement. As a result, it is equally important that the data collected from the diffractometer scan of the sample displays solely it's characteristic x-ray data as a function of theta. To get a spectral scan that obeys this goal, there are other considerations of the x-ray behavior to analyze. The diffraction pattern produced by a spectroscopy will be present; yet there are other theta-dependent properties like Bremsstrahlung curves that must be filtered out of the data to reveal the pure diffraction pattern and the all-important peaks.

2.3. Sources of XRD Error

2.3.1. Uncertainty of X-rays

There are multiple components of uncertainty regarding XRD in general. The first is the uncertainty of the x-ray intensity in respect to number of counts. This source of uncertainty can be modeled by the square root of the total radiation counts at a given angle.

This standard deviation equation adequately fits for the uncertainty in a spectroscopy of x-rays, where the quantity of radiation counts at a given angle is collected over a period of time, and is functionally collecting the rate of x-rays on average over a time span. Then, taking the square root of the count rate at an angle functionally gives the standard deviation of the average, implying the likelihood of counts at a given location having error of one σ from the mean.

2.3.2. X-ray Beam Width

As the x-rays formed in the Norelco x-ray tube are emitted, the quantity of x-rays that enter the collimation tube are described by the ratio,

$$\mathrm{I} = \frac{\pi r^2}{2\pi x^2} = \frac{r^2}{2x^2}, \tag{29}$$

where the values r and x are the radius of the collimation tube and the distance of the collimation tube entrance from the x-ray tube, respectively. Those values are 1.0 cm and 73.0 cm. This ratio would be assuming uniform x-ray intensity from a central point from the x-ray tube source, which isn't correct but provides a starting point for beam width uncertainty. Due to the lead material of the collimation tube, x-rays that are initially off target will be partially absorbed, and their energies will be weak enough upon exit of the tube that their counts will be recorded as background. Then, the number of x-rays who exit the collimation tube are already a far smaller quantity.

The collimation tube acts as filtration for the x-rays who travel off the intended course. Then, the waves that exit the tube will travel 10 cm to the sample, where diffraction will occur. Any waves that travel from the collimation tube to the sample will have a maximal error in entry angle described by the conic shape described by the measurements of the collimation tube, depicted in Figure 14. Collimation Tube Uncertainty Diagram. The uncertainty provided by the width of the maximum x-ray beam on the sample, 2.27 cm, indicates a largely high source of error when the goal is to measure across cross-sectional area of metallic grains in the range of square millimeters.

The implementation of a pinhole cap to the collimation tube will aid in the overall performance of uncertainty minimization in terms of x-ray beam width. Additionally, a cap would lower any background radiation counts experienced by the sensors in the housing chamber. There are other stop guards to mitigate the effects of a wide x-ray beam. The radiation monitor is shielded and has its own pinhole, so only the properly diffracted x-rays of the sample were ideally recorded during experimentation.

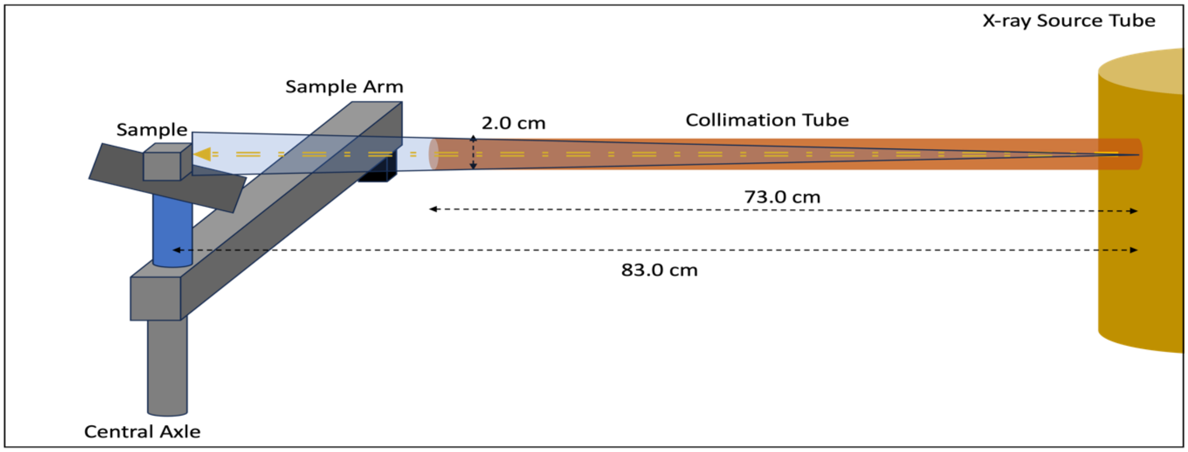

Figure 14. Collimation Tube Uncertainty Diagram. By treating the x-ray source as a point, the similar triangles of the collimation tube width and the x-ray beam indicate a maximum x-ray beam width of 2.27 cm.

2.3.3. Stepper Motor Uncertainty

The source of error that appears easiest to minimize is the stepper motor uncertainty. Due to the XRD protective steel framing necessarily remaining closed during x-ray experimentation, exact location of motors cannot be evaluated. The code block that operates the stepper motors has motor strength coefficients, and these can be manipulated, tested, and observed during experimentation, in the cases that don't produce and record x-rays. The stepper motor error will certainly affect angle-based certainty, and the error bars along the x-axis would for this component of uncertainty are at this point too significant to even be worthwhile in plotting. Due to the quantitative error associated with one step per degree, which is unknown to begin with, the error will increase by the difference between expected step location and actual location for each step of the motors, compounding the rate of error with each movement of the stepper motors. Fortunately, there are potential solutions to these issues, which could be implemented as soon as in a year from the time of writing.

These components of error and their potential minimizations have been considered for future research and analysis. There are instruments that can be appended to the Houghton XRD to eliminate error, specifically in the motor positioning error. While traditional x-ray intensity error is always present, an XRD operating solely under intensity error can be sufficiently precise to evaluate thin films.

Chapter 3: Mechanical Apparatus

3.1. Overview

The apparatus of the XRD can be divided into three sections: the x-ray source and radiation housing unit, the high-voltage electronics, and the digital control systems. The housing unit consists of the sample holder, the collimation tube, and the radiation monitor, all placed on a 180-degree track, and encased in protective steel x-ray-containment panels set with safety interlocks along its edges. The internal structure of the housing unit is pictured in Figure 15. The high voltage electronics float the circuit powering the x-ray source. The digital control systems consist of multiple independent components. First, a computer runs National Instruments LabView coding that directs a dual stepper motor driver to power the two motors that carry the theta and 2-theta around the track of the Housing Unit. A separate computer is timed to record the x-ray counts by time with connection to the radiation monitor via Vernier's Logger Pro software, and the respective angle is calculated manually via the time-step directed code and the timing feature of Logger Pro.

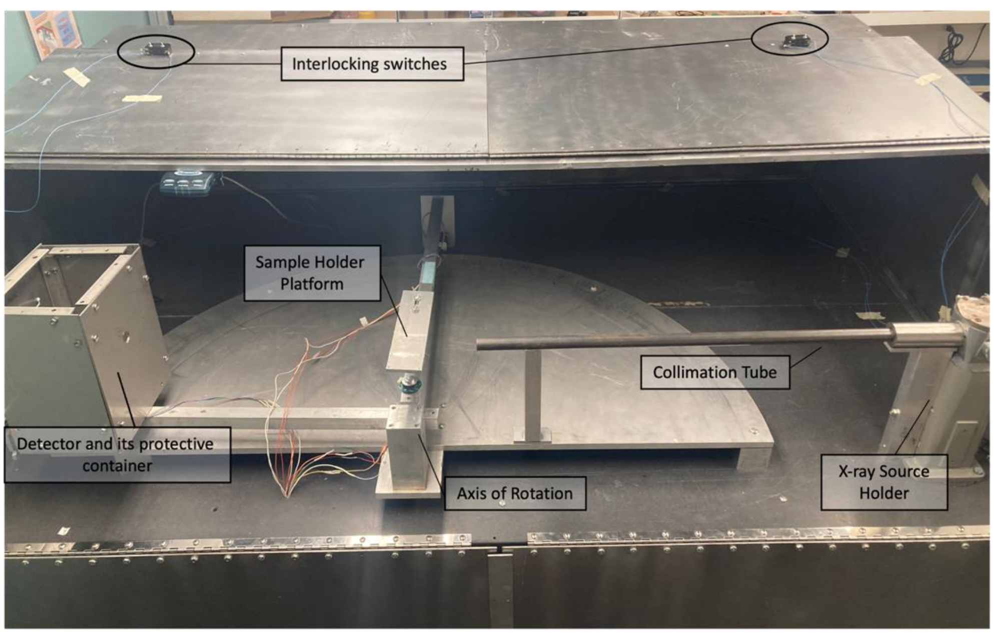

Figure 15. Overhead image of the Houghton University XRD Housing Unit. The stepper motors beneath the Detector Arm and the Sample Arm rotate along the semicircular path, directed from the LabView-running computer terminal located beneath the Housing Unit.

3.2. X-ray Tube and Housing Unit

3.2.1. X-ray Source

The Houghton University XRD utilizes a Philips-Norelco x-ray tube that supplies a characteristic x-ray source, as demonstrated in Figure 16. The target and filament are themselves housed in a glass tube and permanently mounted to a steel block, which is bolted into the x-ray tube housing. The x-ray tube housing is fixed to the table and holds the x-ray tube in place. The x-ray tube housing is fitted with a pathway for the water-cooling system, to provide some resistance to overheating of the copper target. The water-cooling system is rudimentary; a silicone tube with diameter of 0.95 cm runs from a nearby sink, flows water through the x-ray tube housing, and the water returns to the sink. Within the x-ray tube housing, the water flows through two 0.635 cm diameter Cu pipes that pass through the x-ray tube to continuously cool the target during experimentation. The Cu pipes are connected to the x-ray tube by rubber O-rings, and the silicone tubing delivers the water through the x-ray tube housing. Despite its rudimentary design, the cooling system does maintain a low enough temperature within the x-ray tube such that overheating of the target is prevented. As a result, the tube can continue producing x-rays throughout the duration of the apparatus' run.

3.2.2. X-ray Path

Once the x-rays are created, they travel in an upward trajectory through the tube and out of mica and beryllium windows of the x-ray tube, and then through the collimation tube. Then, the x-rays are delivered through the sample, diffracted, and received by the Vernier Geiger meter, the radiation counter of the XRD. This completes the basis of the production and collection of this component of the apparatus. When the x-rays travel out of the collimating tube, they are the only x-rays whose paths are directly on target to the sample, within the constraints of the uncertainty calculations from Section 2.3.2. The sample mount is fixed onto the theta dependent arm. Both the sample arm (Arm 1) and the detector arm (Arm 2) are fixed on one end around a central axis at the tip of the semicircular, 180° angular track. The other end of each arm has one stepper motor each, such that one end of the arm is free to rotate per the motor controls, while the other end remains fixed around the central axis.

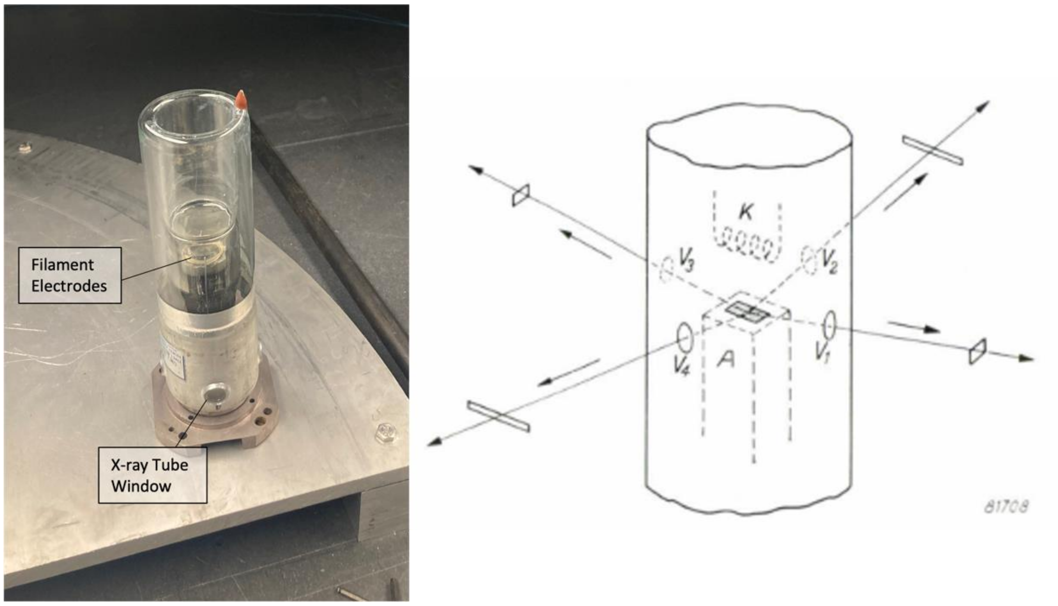

Figure 16. Phillips-Norelco x-ray tube image and diagram.. Left: Houghton's Norelco x-ray tube from the XRD. Right: The Norelco x-ray diffractometer tube that produced x-rays in the Norelco Diffractometer technical design basis (1954). Both diagram and image show the x-ray tube to be upside down compared to their orientation during the experiments. The cathode is heated to produce electrons traveling to the anode to produce x-rays. The produced x-rays then disperse out of each v_i mica and beryllium window in the tube. Diagram on right is taken from Ref. [22].

3.2.3. Sample and Detector Arms

While the sample mount rotates atop Arm 1, Arm 2 has the Geiger Meter attached to its end, reading the x-rays that were diffracted by the sample. The Geiger Meter is encased in an 0.3175 cm thick steel box. The box has one hole of the same radius, 1.25 cm, as the collimating tube, which further aids in the collimation of x-rays. In this manner, the x-rays incident on detector are of known diffracted angle. The steel box aids in protection from background scatter of misaligned diffracted x-rays and decreases background radiation picked up by the monitor. The motors that carry the arms are LIN Engineering NEMA 5718 Hybrid Motors with the original design idea of the arm-carrying motors 'stepping' along fixed intervals The stepper motors are remotely programmed using National Laboratories LabView programming, and each motor has its own 'stepping coefficient' associated with it for variability in testing and consistency. With an apparatus dealing with spectral analysis like a diffractometer then, the usage of discrete stepping motors allows the operator to stop and start the motors at discrete intervals for mathematical analysis, some of which was discussed in Section 2.3.3. Then, the x-rays are diffracted off the sample and received by the Geiger meter. This completes the basis of the components of the apparatus responsible for x-ray production.

3.2.4. Safety Features

The x-ray tube itself is powered through the electronics stations via the circuit that stimulates the cathode with current, so the x-ray tube also heavily relies on Section 3.3 as a driving mechanism for operation. The steel x-ray-containment panels that enclose the Housing Unit were also fitted with interlocking mechanisms, pictured in Figure 17.

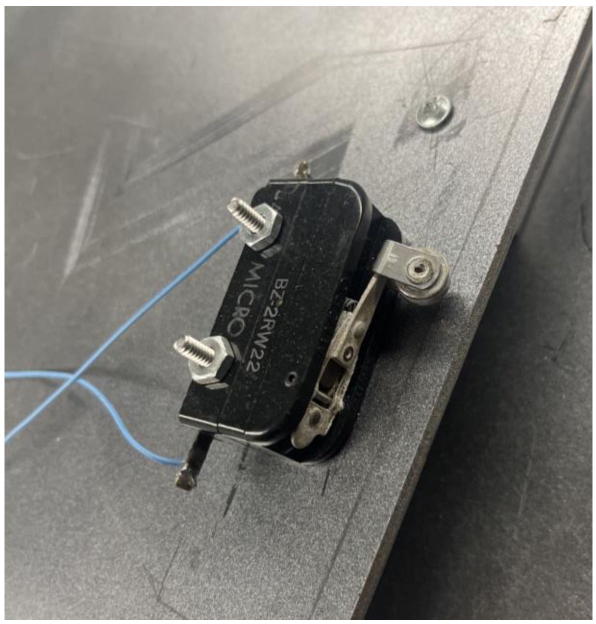

Figure 17. Interlocking Switches Responsible for High Voltage Power Shutoff. The Honeywell MICRO BZ-2RW22 safety switches are attached to each mechanical opening panel on the XRD Housing, and each switch must be closed for the High Voltage Power source to power on.

The Honeywell interlocking safety switches are connected to the "HiTek Power Series 1000" High Voltage power supply of the apparatus. When any switch was opened, the high-voltage was shut-down in all capacities. Then, if any panels are remained open during experimentation, or attempted to open, the system is designed to shut-down x-ray production instantaneously. These locks surrounding the exterior of the Housing Unit are important safety measures installed to ensure radiation received by the experiment operators are minimal to none.

3.3. Electronics

There are primarily two components of the electronics for the x-ray source. The circuit that delivers current to the x-ray tube to heat the filament is aptly called the filament circuit, and the entire filament circuit is itself floated by the aforementioned High Voltage power supply.

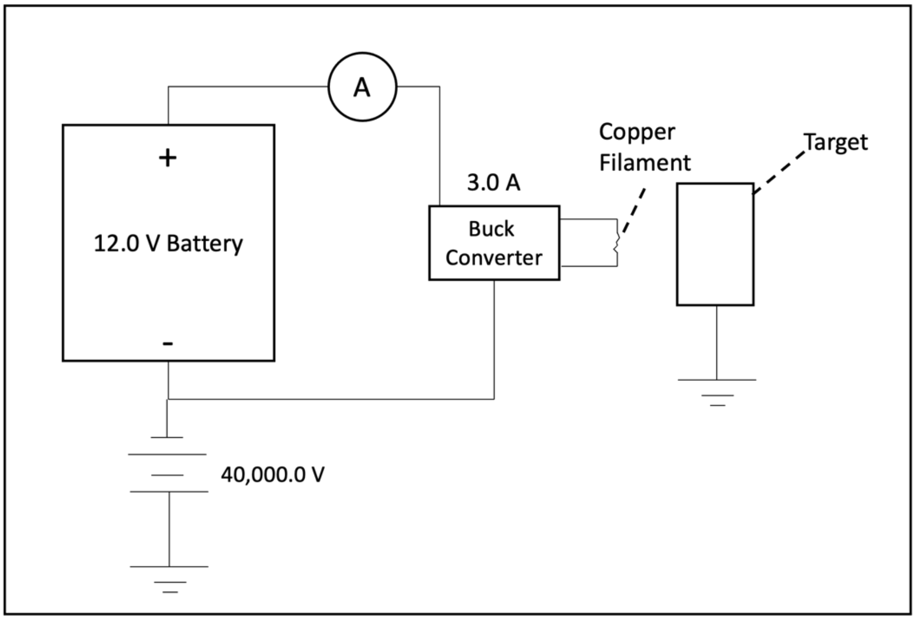

Figure 18. X-ray source power circuit diagram. The 12 V battery provides the current to stimulate the copper filament. The buck converter maintains a current of 3.0 A passing through it, and the current is passed through the filament to heat it. The electrons stimulated enough to travel from the filament to the target are further propelled by the voltage drop of the entire filament circuit (40kV).

The filament circuit, pictured in Figure 18, is operated from within a sterilized plexiglass containment box. The electronic containment is a 0.635 cm thickness box within which much of the high voltage necessary for floating the x-ray circuit is. The chamber contains a 12 V battery, for supplying a potential difference over the x-ray tube circuit. The circuit is necessary to create a system in which electrons flow in the direction of the x-ray filament. As discussed in the x-ray Tube and Housing section, the x-ray tube circuit is floated at magnitudes of up to 40,000 V. For the electrons that are flowing through the circuit to have enough energy to bombard the target and produce an x-ray, the floating voltage of 40K is required to stimulate the electrons sufficiently.

The circuit includes a Droking 3.0-A buck converter, which serves multiple purposes in the x-ray tube circuit. The circuit is dependent on current-controlled input, of which the x-ray tube filament has a maximum of 3.0 A. Further magnitude of current placed over the circuit would cause the filament of the x-ray tube to burn out. The buck converter acts as the current control of the circuit, and additionally acts as a voltmeter. The outputs of both voltage and current remain solely on the output of the buck converter but are easily read from outside the electronic box in the user control interface area. The filament current is the component of the circuitry that produces enough heat in the filament such that the electrons are ejected from the filament. A fixed filament current is necessary for the efficacy of the XRD, so the filament current must remain constant throughout the duration of an experiment.

As previously stated in Section 2.1.2, there is a direct relation between intensity and x-ray production. The electrons that produce x-rays require sufficient heating of the filament via delivering the current of the circuit to be stimulated sufficiently to a large enough magnitude of velocity. To aid in the delivery of electrons from the filament to the Cu target, a drop in voltage is utilized. Thus, the filament circuit is floated at high voltage. The voltage that is found to be optimal for x-ray emission can be summarized as 40 kV, with some room above that number giving peak intensity. Due to the high voltage floating the circuit, there is an upper limit to peak characteristic x-ray production while also minimizing the rate of Bremsstrahlung radiation, though that quantity is difficult to acquire without damaging the filament's integrity. The high voltage, supplied by the HiTek High-Voltage power supply, is controlled by an RSR Hy3003 DC Power Supply.

3.4. Digital Control Systems

The Houghton XRD is operated almost entirely by the LabView computer program. The LabView program controls the operation of the 2 stepper motors of the Arms of the XRD, which is no longer in active use. The two arms are controlled by National Instruments Stepper Motors, which are coded to move as directed via LabView programming. The LabView code has been replaced with Arduino operating code, with hopes of long-term increase in stepper motor consistency. Additionally, two encoder rings, mounted to each arm, monitor the rotation of each arm with a precision equal to a third of a degree, though still needs to be quantitively tested.

For the collection of data, Logger Pro Software Program is used to read the number of radiation counts. During the collection period, the LabView program is initiated at the same time to begin a collection period with the Logger Pro's program, run on a separate computer. The counts are then tabulated with a stepped collection period of variable length, but most prominently ranging 20 seconds per angle.

Chapter 4: XRD Results and Analysis

4.1. Results

Throughout the experiment's existence, the primary objective has predominantly been to produce spectroscopies of a sample. The reasoning for this goal would be that once the apparatus was found to be sufficiently 'working' on a macroscopic scale, the fine tuning and specificity required for XRD results to mean anything could thereby follow. During the summer of 2021, the first 'successful' scan of the Houghton XRD took place since 2017, as depicted in Figure 19. The scan in 2021 was a single-spectral recording of an unknown substance, taken over the time of approximately 8000 seconds. The scan depicts a smooth relation to the expected Bremsstrahlung radiation curve produced via intensity-angle relation discussed in Section 1.2. Though the overall counts are low, there are two peaks on the spectral scan that are of interest. The peaks are beyond the limits of experimental error at angles $\theta = 62.2°$, and $\theta = 69.0°$. These peaks have been experimentally found to belong to Silicon in the orientation index called 100, which would align with the samples in the laboratory's possession.

During the same experiment, the maximal number of radiation counts recorded were 76500 counts. Furthermore, relatively consistent counts were recorded throughout the duration of the scan, after the arms had moved far enough from starting position. The radiation counts then imply the maintained alignment (Arm 1 moving at half the distance per uniform motor step of Arm 2) between Arms 1 and 2 throughout the duration of the experiment. This is one area of concern regarding reproducibility of the experiment; the alignment of the stepper motors seems to inconsistently operate as their coding constitutes. The stepper motor misalignment may be one form of experimental error that limits reproducibility of the XRD, but there are 2 other components, the sample stage and the sparking issue, that must also be addressed before the results produced by the Houghton XRD are reliable and consistent.

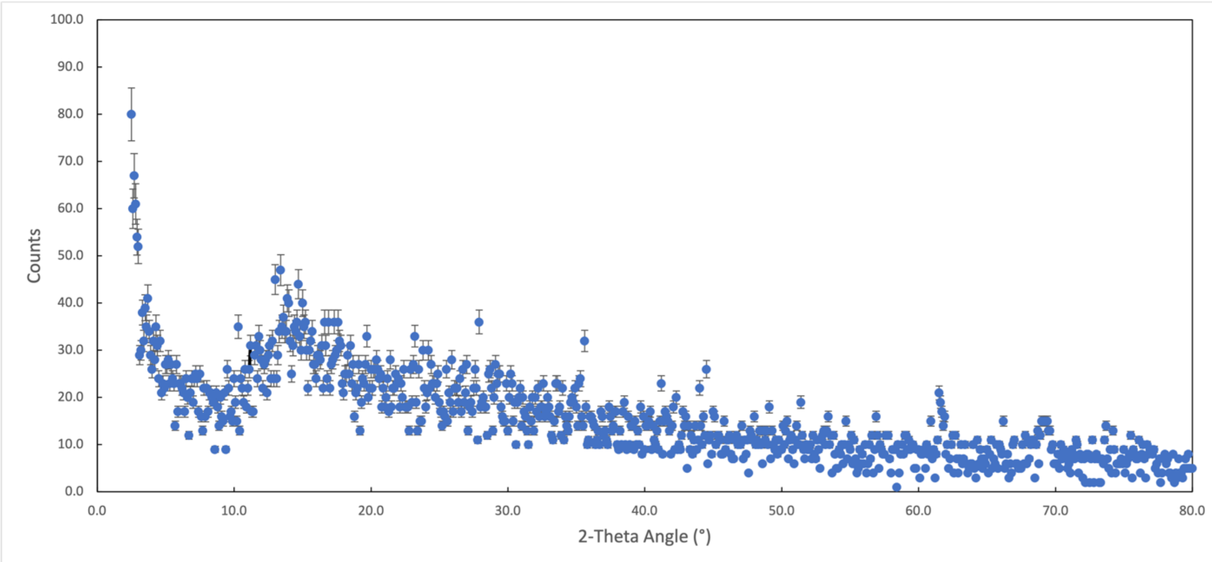

Figure 19. Successful scans of the Houghton XRD, 2021. The scan shown here is a Silicon-100 spectroscopy to distinguish the Bragg-angle peaks that differentiate from background noise. Duration of 8000 seconds recorded, with single-spectrum stepper motor operating every 0.1 degree with 10 second intervals. Spectroscopy of sample measured from 0.0° – 80.0°.

4.2. Current Status

The Houghton XRD is operational as an apparatus, but not yet useful for research. There are components of fine tuning that can be implemented to increase the quality of results found by the XRD. The radiation counts of the successful scan on June 25, 2021 were at their highest recorded in terms of peaks eclipsing background radiation. However, there was an issue of sparking occurring during the scanning process. Roughly 1900 seconds into the experiment, and occurring again at 2000 seconds, the buck converter in the beam circuit was found to be experiencing significant sparking. Due to the buck converter's current flow being set to 3.1 A, along with the beam circuit's floating voltage of 40 kV, the tight circuitry of a Droking Buck Converter makes it a prime location for loose electrical sparks to be formed through the medium of air itself. The electric field formed by the floated circuit reaches a level of dielectric field strength such that the dielectric breakdown strength of air (3 kV/mm) is bypassed and a channel from one point on the circuit is connected to another, emitting a bright flash and loud pop of dissipating electricity. These pops instantaneously lower the floating voltage and current of the beam circuit, which lower the radiation counts occurring directly after the instance of sparking. For this reason, it would be beneficial to eliminate the sparking problem in and around the buck converter. The buck converter would not be the cause of sparking. At some location in the circuit box, a connection to ground was created, instantaneously grounding the Buck Converter, eliciting a spark. It is unknown where the origin of the circuit box's grounding is located, but greater care will have to be taken to both preserve long-time operation of the Buck Converter and return consistent x-ray intensity during experimentation.

Some tests that could help in reducing likelihood of sparking occurring in the electrical setup would be regarding finding maximal floating voltage needed to produce sufficient x-rays for operation. An experiment could be completed relating floating voltage of the circuit and x-ray count, where the energy is incrementally increased until counts stabilize to determine the threshold floating voltage of the system. This experiment could twofold in intent; the threshold floating voltage being a primary component, but also determining the XRD's ability to produce stable intensity as other variables (beam circuit voltage and current) are manipulated. There is intuitively a tradeoff taking place when considering the voltage to float a circuit over; within the confines of realistic voltages able to be acquired in this experiment, the higher the floating voltage, the higher the voltage drop between beam circuit and copper target, and the higher the radiation counts will be found. However, the floating voltage is a primary reason that the dielectric breakdown threshold is passed. Tests to determine some of the components mentioned would be simple to initiate, and the results would reveal new capabilities of the XRD that were previously considered unlikely.

4.3. Future Plans

There are a series of experiments lined up to evaluate the performance of the XRD. First, the high-voltage tests must be conducted to examine the replicability of the results. Additionally, the problem of the misalignment of the stepper motors during experimentation was previously discussed. While multiple experiments were performed during the summer of 2021, there was a clear discrepancy of radiation counts between them. The mechanical quantities of the experiments were held constant, so the only component of the apparatus that would change during experimentation is the placement of the arms and sample.

As a result of this implication, it was concluded that encoders must be placed onto the axes of Arms 1 and 2 to verify the locations of the arms with a second source of accountability. As seen in Figure 20, two CALT GHH60 rotary encoders have been installed on each arm and are now being tested. These experiments should account for the uncertainty in stepper motor angle. A correction function will be implemented into code to keep the stepper motors of the arms at the desired angle.

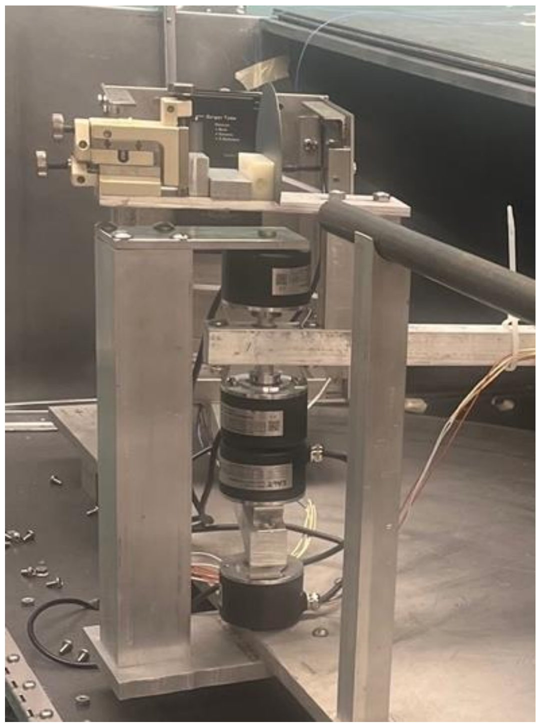

Figure 20. Encoders Placed onto Arms 1 and 2. The magnetic encoder rings will monitor magnetic flux via rotation of the arms about the central axle. Then, the encoders will offer a quantitative 'check' to the stepper motor alignment, optimally aiding in minimizing stepper motor error. While encoders have been minimally tested, theoretically the encoders should be able to monitor as precise as a 0.33° motor step.

Another component to be revisited in the future is the source of power for the beam circuit. Currently, a 12.6 V capacity battery is used to power the circuit. This isn't the most effective source of power as the batteries require re-charging externally from the circuit and its container. To perform longer duration testing that the XRD may require, the battery must be replaced in one way or another. Additionally, the battery must be removed from the circuit and taken out of the decontaminated and sterile circuit box. This removal leads to potential contaminants entering the box and prompts a cleaning of the box between experiments. To increase the turnaround time between experiments and increase the duration of potential experiment runtimes, an alternative source of power capable of delivering 3V to the circuit is being explored.

One such solution to this problem would be the implementation of a magnetic induction-powering transformer to become the power source. In this way, power could be delivered externally from the circuit box by a rotating magnet while the wiring and voltage would be delivered into the box. In the pursuit of such a means of power, a homemade transformer was developed, with its circuit diagram below in Figure 21.

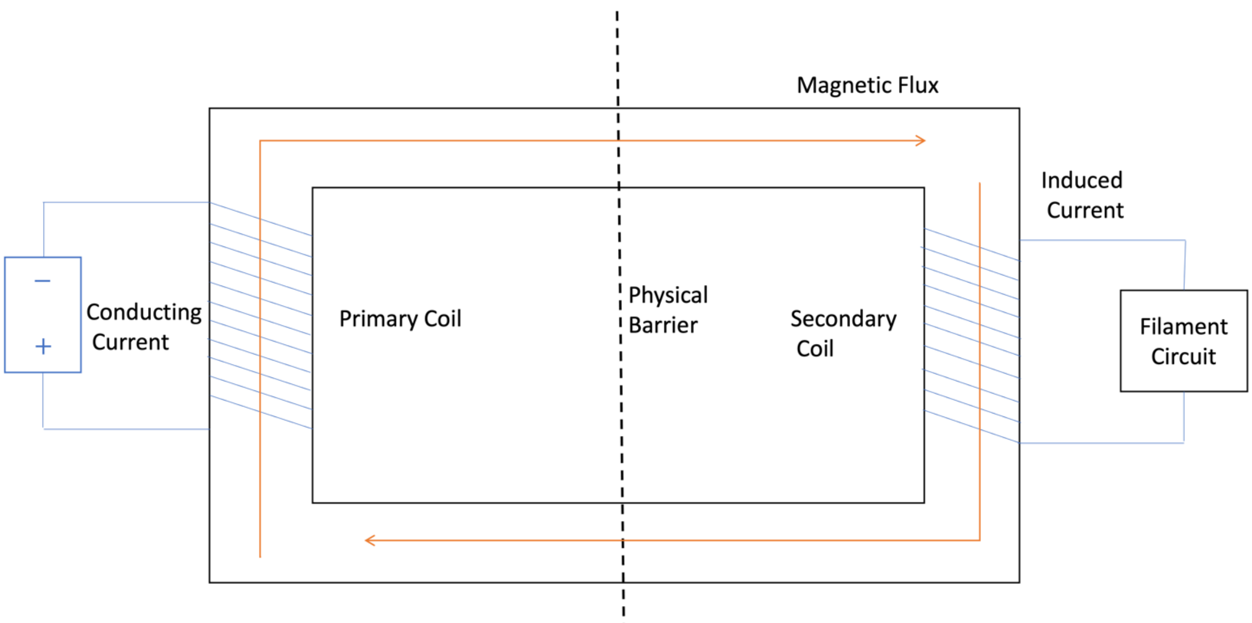

Figure 21. Circuit Diagram of Transformer Prototype. The conducting current is produced by a DC power source. The current flowing through the solenoid of the primary coil induces a magnetic flux through the transformer core, which in turn induces current into the secondary coil, thus powering the filament circuit. The filament circuit will be powered by alternating current, but implementation of rectifying diode could return the filament circuit to regulated current. If the transformer core can be integrated seamlessly into the physical barrier, the Circuit Box in the case of the Houghton XRD, the filament circuit can be powered.

The transformer has thus far yielded little in quantitative results. While alternate current was measured briefly in testing, the output was low and non-sinusoidal, but instead peaking randomly when tested against magnet flux and angular velocity. Further testing and development will be required to develop a suitable and sufficiently powerful transformer for the specifications of the beam circuit. Additionally, the transformer would require changes to the components of the beam circuit. The primary change would be to return DC power from the transformer's delivery of AC current. This would simply require a rectifier placed between the power source and the rest of the circuit. A rectifier of such quality for the beam circuit could simply be purchased and would also pose the additional benefit of regulated DC power at a higher consistency than the 12.6 V battery currently being utilized.

The final component to be explored for the XRD to gain precision and long-term efficacy is a sample mount that can be operated to move remotely. When the Houghton XRD reaches status that reproduceable experiments can be conducted, the goal of the XRD will transition to being able to find inconsistency in the thin films produced by the deposition chamber. This would require the thin films to be mobile in some capacity when experimentation is underway, such that the sample's cross-sectional area can be measured. At the phase of progress it was left, the sample mount was nothing more than a platform with an abrasive surface to avoid slipping of the sample upon rotation. An ideal sample mount would be able to be externally operated to move both laterally and vertically to the path of incoming x-rays. The plan to implement such a stage has only been discussed in theory with some exploration of options to purchase. However, the problems that such a stage's implementation would solve cannot yet be analyzed until the overall precision of the apparatus has been increased. As a result, this component of improvement takes less precedence than the encoder installment and filament circuit power source.

The overall status of the Houghton XRD was operational by end of undergraduate period. While there are various sources of error, the systems in place to be constructed and tested could develop the apparatus to be able to produce replicable results in the coming years. Ideally, the Silicon-100 scan can be preproduced with more quantitative peaks observed at the Bragg angles. A successful scan in that vein would imply the enhancement of precision. At that point, the apparatus could be explored in the pursuit of thin film analysis on a macroscopic level.

References

[1] W. C. Roentgen. On a New Kind Of Rays. Phys. Med. 64**. 3-13. (**1895).
[2] J. J. Thomson. Cathode Rays. 77–101. (1897).
[3] Deutsches Röntgen Museum, *Starting the expedition*, WWW document, (https://roentgenmuseum.de/en/home-en/).
[4] Taylor J. The X-ray History of a Fracture. Bristol Med Chir J (1883). 1900 Sep;18(69):214-216. PMID: 28897859; PMCID: PMC50624.
[5] P.P. Ewald. 50 years of X-ray Diffraction. 192-242. (1962).
[6] W. Friedrich, P. Knipping, M. Laue, Sitzungsber. K. Bayer. Akad. Wiss. Math. Phys. Kl. 1912, 303–322.
[7] Presentation.Nobelprize.org. Nobel Prize Outreach AB. Wed. 3 Apr 2024. (1912 Speech, Unpublished).
[8] W. Friedrich, P. Knipping, M. Laue, Sitzungsber. K. Bayer. Akad. Wiss. Math. Phys. Kl. 1912, 303–322.
[9] Bragg, W. L. (1913). The Structure of Some Crystals as Indicated by Their Diffraction of x-rays. In Source: Proceedings of the Royal Society of London. Series A, Containing Papers of a Mathematical and Physical Character (Vol. 89, Issue 610).
[10] Newton Sir Isaac. Axioms, or Laws of Motion, Principia Mathematica. (1687).
[11] W. H. Bragg, W. L. Bragg. The Reflection of x-rays by Crystals. (1913).
[12] F.H. Crick. The structure of DNA. In The Medical Research Council Unit for the Study of the Molecular Structure of Biological Systems, The Cavendish Laboratory, Cambridge, England (Vol. 59, Issue 6, pp. 569–571). American Medical Association. https://doi.org/10.1001/archpsyc.59.6.569. (1955).
[13] R. Franklin, Photo 51. https://www-project.slac.stanford.edu/wis/images/photo_51.jpg (1952).
[14] Wood, W. A. Proc. Phys. Soc. 44 67 (1932).
[15] Faraday, M. Terrestrial Magneto-Electric Induction, T. B. L. Experimental Researches In Electricity. HTTPS://ROYALSOCIETYPUBLISHING.ORG/. (1832).
[16] Meza, E. PV Magazine Online Article. https://www.pv-magazine.com/2014/04/24/tesla-partners-with-hanergy-on-first-chinese-charging-stations_100014889/. (2014).
[17] Berkmire, Hanket, Russell, Wendt. Thin-Film, Flexible Photovoltaic Module. US 6,310, 281 B1. (Oct. 30, 2001).
[18] S. R. Baker, D. B. Hoffman, et. al. Texture transformations in Ag thin films. Elsevier 61 7121 (2013).
[19] J. M. Malone. Undergraduate Thesis (Houghton College, New York, 2021, unpublished).
[20] H. C. Phillips. Undergraduate Thesis (Houghton College, New York, 2018, unpublished).
[21] B. D. Cullity, S. R. Stock, General Physics Textbook with Modern Physics. (2014).
[22] Parrish, W., Hamacher, E. A., & Lowitzsch, K. The “Norelco” x-ray Diffractometer. (1954).